0.3 T, the composite films had a flatter dependence on applied field, and the absolute values of J_c began to increase with respect to 123 films. The self-field J_{ct} of the composite films were increased to above 4 MA cm^{-2} from initial results of 2–3 MA cm^{-2} (ref. 21). The increase of the self-field J_c was achieved by decreasing the 211 particle deposition time and hence the 211 'pseudo' layer thickness from 1–1.5 nm to 0.5 nm. A decrease of 211 'pseudo-layer' thickness from 1.0 nm to 0.5 nm increases the volume percentage of the 123 phase and presumably reduces the intrinsic stresses of the 211/123 composites. This decrease in thickness of 211 also increased the T_c from 88.9 ± 0.2 K to 90.2 ± 0.4 K on average (for a layer thickness of ~11 nm for 123). These factors combined potentially enhance the zero-field J_c. ☐

1. Bednorz, J. G. & Muller, K. A. Possible high T_c superconductivity in the Ba-La-Cu-O system. *Z. Phys. B* **64**, 189–193 (1986).
2. Wu, M. K. *et al.* Superconductivity at 93 K in a new mixed-phase Y-Ba-Cu-O compound system at ambient pressure. *Phys. Rev. Lett.* **58**, 908–910 (1987).
3. Larbalestier, D., Gurevich, A., Matthew Feldmann, D. & Polyanskii, A. High-T_c superconducting materials for electric power applications. *Nature* **414**, 368–377 (2001).
4. Matsushita, T. Flux pinning in superconducting 123 materials. *Supercond. Sci. Technol.* **13**, 730–737 (2000).
5. Civale, L. *et al.* Vortex confinement by columnar defects in YBa$_2$Cu$_3$O$_7$ crystals: enhanced pinning at high fields and temperatures. *Phys. Rev. Lett.* **67**, 648–651 (1991).
6. Selvamanickam, V. *et al.* Fabrication of 100 A class, 1 m long coated conductor tapes by metal organic chemical vapor deposition and pulsed laser deposition. *Physica C* **392–396**, 859–862 (2003).
7. Verebelyi, D. T. *et al.* Uniform performance of continuously processed MOD-YBCO-coated conductors using a textured Ni-W substrate. *Supercond. Sci. Technol.* **16**, L19–L22 (2003).
8. Groves, J. R. *et al.* Recent progress in continuously processed IBAD MgO template meters for HTS applications. *Physica C* **382**, 43–47 (2002).
9. Goyal, A. *et al.* Recent progress in the fabrication of high-J$_c$ tapes by epitaxial deposition of YBCO on RABiTS. *Physica C* **357–360**, 903–913 (2001).
10. Balachandran, U. *et al.* Development of coated conductors by inclined substrate deposition. *Physica C* **392–396**, 806–814 (2003).
11. Kakimoto, K., Iijima, Y. & Saitoh, T. Fabrication of long-Y123 coated conductors by a combination of IBAD and PLD. *Physica C* **392–396**, 783–789 (2003).
12. Yamasaki, H., Nakagawa, Y., Sawa, A., Obara, H. & Develos, K. Flux pinning effects of twin boundaries studied with unidirectionally twinned YBCO films. *Physica C* **372–376**, 1885–1889 (2002).
13. Feenstra, R., Christen, D. K., Klabunde, C. E. & Budai, J. D. Role of oxygen vacancies in the flux-pinning mechanism, and hole-doping lattice disorder in high-current-density YBa$_2$Cu$_3$O$_{7-x}$ films. *Phys. Rev. B* **45**, 7555–7558 (19931992).
14. Larbalestier, D. C. & Maley, M. P. Conductors from superconductors: conventional low-temperature and new high-temperature superconducting conductors. *MRS Bull.* **18**, 50–56 (Aug. 1993).
15. Dam, B. *et al.* Origin of high critical currents in YBa$_2$Cu$_3$O$_{7-x}$ superconducting thin films. *Nature* **399**, 439–442 (1999).
16. Pan, V. M. *et al.* Nature of magnetic field and angular dependencies of the critical current density in epitaxial HTS YBa$_2$Cu$_3$O$_{7-x}$ films. *Physica C* **388–389**, 431–432 (2003).
17. Reichelt, K. Nucleation and growth of thin films. *Vacuum* **38**, 1083–1099 (1988).
18. Redl, F. X., Murray, K.-S., Cho, C. B. & O'Brien, S. Three-dimensional binary superlattices of magnetic nanocrystals and semiconductor quantum dots. *Nature* **423**, 968–971 (2003).
19. Springholz, G., Holy, V., Pinczolits, M. & Bauer, G. Self-organized growth of three-dimensional quantum-dot crystals with FCC-like stacking and a tunable lattice constant. *Science* **282**, 734–737 (1998).
20. Liu, P., Zhang, Y. W. & Lu, C. Self-organized growth of three-dimensional quantum-dot superlattices. *Appl. Phys. Lett.* **80**, 3910–3912 (2002).
21. Haugan, T. *et al.* Island-growth of Y$_2$BaCuO$_5$ nanoparticles in (211$_{~1.5 nm}$/123$_{~10 nm}$)xN composite multilayer structures to enhance flux pinning of YBa$_2$Cu$_3$O$_{7-δ}$ films. *J. Mater. Res.* **18**, 2618–2623 (2003).
22. Gross, R. E. & Campbell, A. M. Numerical calculation of elastic pinning parameters by point pins. *Physica C* **260**, 188–196 (1996).
23. Haugan, T., Barnes, P. N., Brunke, L., Maartense, I. & Murphy, J. Effect of O$_2$ partial pressure on YBa$_2$Cu$_3$O$_{7-δ}$ thin film growth by pulsed laser deposition. *Physica C* **297**, 47–57 (2003).
24. Zhu, Y., Cai, Z. X., Budhani, R. C., Suenaga, M. & Welch, D. O. Structures and effects of radiation damage in cuprate superconductors irradiated with several-hundred-MeV heavy ions. *Phys. Rev. B* **48**, 6436–6450 (1993).

Competing interests statement The authors declare that they have no competing financial interests.

Correspondence and requests for materials should be addressed to T.J.H. (timothy.haugan@wpafb.af.mil).

Direct evidence for atomic defects in graphene layers

Ayako Hashimoto[1]**, Kazu Suenaga**[1]**, Alexandre Gloter**[1,2]**, Koki Urita**[1,3] **& Sumio Iijima**[1]

[1]*Research Center for Advanced Carbon Materials, National Institute for Advanced Industrial Science and Technology (AIST), Tsukuba, 305-8565, Japan*
[2]*Laboratoire de Physique des Solides, CNRS UMR 8502, Université Paris-Sud, Orsay, 91405, France*
[3]*Graduate School of Science and Technology, Chiba University, Chiba, 263-8522 Japan*

Atomic-scale defects in graphene layers alter the physical and chemical properties of carbon nanostructures[1,2]**. Theoretical predictions have recently shown that energetic particles such as electrons and ions can induce polymorphic atomic defects in graphene layers as a result of knock-on atom displacements**[3,4]**. However, the number of experimental reports on these defects is limited**[5,6]**. The graphite network in single-walled carbon nanotubes has been visualized by transmission electron microscopy (TEM) and their chiral indices have been determined**[7,8]**. But the methods used require a long image acquisition time and intensive numerical treatments after observations to find an 'average' image, which prevents the accurate detection and investigation of defect structures. Here we report observations *in situ* of defect formation in single graphene layers by high-resolution TEM. The observed structures are expected to be of use when engineering the properties of carbon nanostructures for specific device applications.**

Pentagon–heptagon pairs[9], mono-vacancies and multi-vacancies[4,10–13] and adatoms[3,14] are typical stable graphene defects that have been predicted. (The metastable interstitial-vacancy defect described in ref. 13 is between two graphene planes and is therefore not exactly the same defect as that investigated here.)

We fabricated a desired contrast transfer function (CTF) that enables selective visualization of the graphitic network (see Methods and Supplementary Figs S1 and S2). Under this experimental condition, each zig-zag chain should turn up as a dark line in TEM images and a bright spot should appear in the middle of each hexagonal carbon ring (see Fig. 1a and inset).

In a perfect single-walled carbon nanotube (SWNT; Fig. 1a, b), the moiré pattern formed by the rolled-up graphene layer is clearly visible between two intense dark lines corresponding to the vertical tube walls. By using optical diffraction (Fourier transform), two symmetric hexagons are identified on the tube axis (Fig. 1b inset). Each hexagon in Fourier space corresponds to a single graphene layer (front or back of the SWNT) and represents the orientation of the zig-zag chain as illustrated in Fig. 1a (inset) to the tube axis, from which the apparent chiral angle can easily be deduced[15]. The apparent chiral angle and the tube diameter measured in the high-resolution TEM (HR-TEM) image provide one or at most three solution(s) of the chiral index (n, m) for the nanotube under examination. Consequently, the chiral index of SWNT has been assigned as (13, 8) (Fig. 1c) (or (13,7) or (12, 8) with pessimistic error bars).

Such an analysis can be performed even on a SWNT of mixed chirality (Fig. 1d). This non-uniform SWNT was produced by electron bombardment, as described in previous[16,17] reports of processes used to thin the walls of SWNTs. Optical diffraction analysis of the SWNT tells us that the tube with an axial heterojunction is assigned to (17, 0) at the upper part and (18, 0) at the lower part. It implies that this serial junction created in situ here consists of a semiconducting (17, 0) SWNT and a metallic (18, 0) SWNT, and then may generate a nanodiode. A pentagon–heptagon pair is most probably responsible for the serial junction of two parts of SWNTs with different chiral indices. An image simulation of an

adjacent pentagon and heptagon (depicted in Fig. 1e, f) fits quite well with the defective region in the observed image. Direct imaging of the graphitic network allows the local analysis of chiral index of composite nanotubes, which other assignment techniques such as Raman or fluorescent spectroscopy are unable to provide.

Such a topological defect can be seen more clearly in a plan view of graphene layers. Next we show the topological defects induced in a single graphene layer observed *in situ* by HR-TEM. Figure 2a shows a plan view of a graphene layer in a carbon nanostructure with a large diameter[18]. After several tens of seconds of irradiation with an electron beam, a missing row of zig-zag chain was clearly observed in the graphene network (compare Fig. 2a (before irradiation) with Fig. 2b (after irradiation)). Such a basal plane dislocation in the graphene layer can be explained by the existence of a topological defect[2]. The pentagon–heptagon pair is one of the reasonable defect models from the viewpoint of energetic stability and can be induced in a graphene layer through the Stone–Wales (SW) process as illustrated (Fig. 2c)[9]. Shown in Fig. 2d is a simulated HR-TEM image of the graphite network with a pentagon–heptagon pair, which agrees quite well with the experimentally observed image. A large cluster of up to 500 atoms has been built for the HR-TEM image simulations. Defect structures were first relaxed by using a semi-empirical potential. In the vicinity of the defect we

used the *ab initio* relaxed structure within this large cluster in the literature[2]. The rows of zig-zag chains in three directions cannot all be seen in the HR-TEM images (Fig. 2a, b) because the graphene layer is largely inclined against the incident beam beyond the limit of the inclination angle ($\sim$20° in this experiment), where the projected spacing of the graphite network goes off the range of the targeted CTF peak. The extent of the local strain field, as defined by loss of contrast in the HR-TEM images, is estimated at about 1.2 nm. Qualitatively, this fits well with the HR-TEM simulation based on the relaxed pentagon–heptagon structure showing a blurred area of 1 or 2 nm around the dislocation core (Fig. 2d). During the formation of this topological defect, an elastic deformation or a bending of the graphene layer can be observed in the time-sequential HR-TEM images. This proves that the SW transformation should have a key role in nanotube relaxation under strain, as previously suggested by a theoretical prediction[19].

Imaging a point defect, such as an atomic vacancy, on a graphene layer is even more challenging and is of crucial importance because it refers directly to the physical and even the magnetic properties of this material[14,20]. Until now, only scanning probe microscopy has been able to investigate the structure of such defects at the scale of an individual object or of a sparse collection of objects[21,22]. Figure 3a, b shows two HR-TEM images of a unique graphene layer, extracted at $t = 0$ s and $t = 320$ s from a series of hundreds of images. It is evident that several white spots have appeared under electron irradiation, and more than six spots could undoubtedly be isolated from the noise level, leading to a crude estimation of about 0.3 point defects per nm^2 in a graphene layer (see Supplementary Movie 1). The cross-section estimated from this experiment is 160 barn ($160 \times 10^{-10} nm^2$), which is quite close to a theoretical value found in ref. 20 for an atom displacement (180 barn). The three
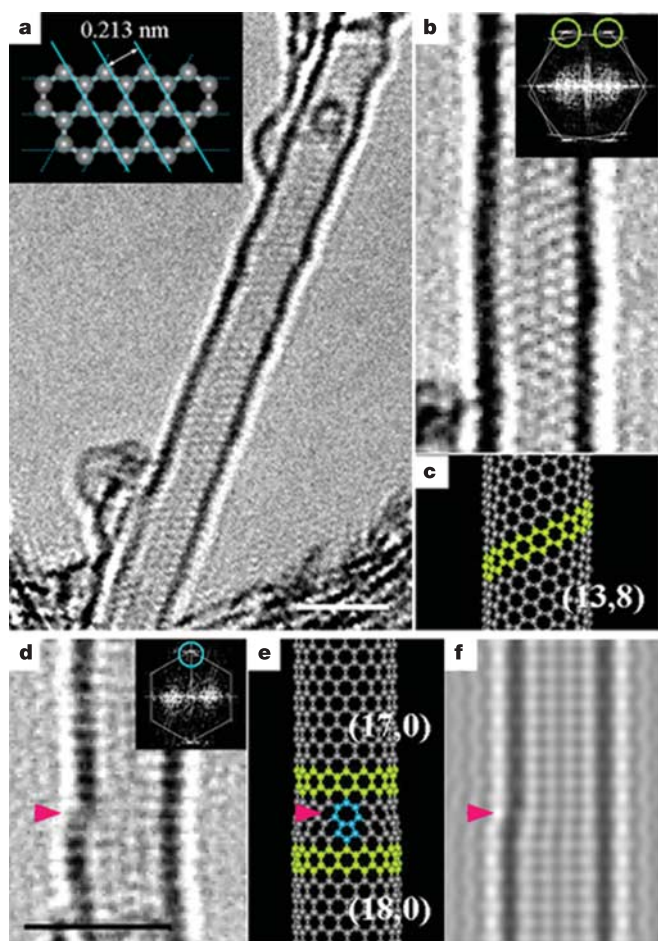

Figure 1 Chiral index determination of SWNTs. **a**, **b**, Chiral index determination of a SWNT. **a**, A typical HRTEM image of a SWNT with enhanced contrast of the zig-zag chain (inset). **b**, Moire pattern and its optical diffraction (inset). **c**, A best-fit model of the SWNT with the determined chiral index (13, 8). **d**, A cross-sectional view of a topological defect at the side of a SWNT. **e**, A pentagon–heptagon pair is presumably responsible for the defect structure and generates a serial junction of two zig-zag nanotubes (17, 0) and (18, 0). **f**, A simulated image for the SWNT with the defect rotated by 90°. Scale bar, 2 nm.
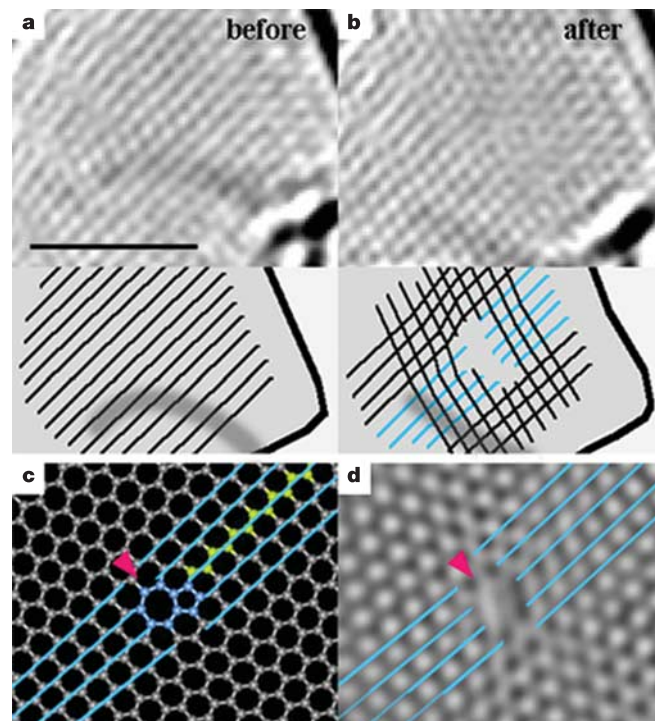

Figure 2 *In situ* observation of a topological defect induced in a graphene layer. **a**, **b**, HR-TEM images of a single graphene layer with a topological defect induced by electron irradiation (before (**a**) and after (**b**)). An edge dislocation is unambiguously visible at the middle of the network where one zig-zag chain is missing through it. The missing zig-zag chain is shown schematically in the bottom part of each panel. **c**, An atomic model of the pentagon–heptagon pair in the graphitic network. **d**, A simulated HR-TEM image shows a good comparison with the HR-TEM image showin in **b**. Scale bar, 2 nm.

neighbouring defects are presented with increased contrast as an inset to Fig. 3b. The intensity profiles are also presented at the position of these three defects in both images for the initial and final states (Fig. 3a, b, inset). In the initial state, the profile shows only the modulation due to the zig-zag chains, with a periodicity close to 0.213 nm. After irradiation, this modulation is more difficult to perceive because of the lattice disorder arising from the point defects[23]. In contrast, these defects appear strongly within the intensity line. HR-TEM simulations have been performed to predict the contrast arising for the most expected point defects on a single graphene layer. In Fig. 3c, d the HR-TEM contrast for one carbon atom vacancy (V_1), two neighbouring vacancies (or an intraplanar di-vacancy, V_2), a pentagon–octagon–pentagon (5–8–5) defect and a carbon adatom can be seen. In Fig. 3c, the atomic positions of the carbon atoms in the vicinity of the mono-vacancies and di-vacancies have not been reconstructed. Nevertheless, theoretical studies[11,24] have predicted that intraplanar relaxation is weak for a mono-vacancy and, indeed, no difference has been seen in our HR-TEM simulation with the use of either relaxed or unrelaxed atomic positions. In contrast, an interplanar di-vacancy can strongly reconstruct and transform to an agglomeration of non-hexagonal rings such as the 5–8–5 defect shown (Fig. 3c). The adatom has also been positioned in the theoretically predicted equilibrium structure—that is, to be in a bridge-like structure—between two surface atoms[3,14]. The major issue of the HR-TEM simulations is that, even for a mono-vacancy, the contrast might be strongly enhanced at the centre of the neighbouring hexagons. This 'delocalization' effect is particularly strong at the chosen defocus. The three point defects imaged (Fig. 3b) can then be simulated by the removal of only three carbon atoms from a graphene layer as shown (Fig. 3e) and we were unable to obtain a better match by using various other types of (multi)-vacancies or non-hexagonal clusters. This demonstrates the sensitivity of HR-TEM to a single carbon vacancy and strongly suggests that the mono-vacancy does indeed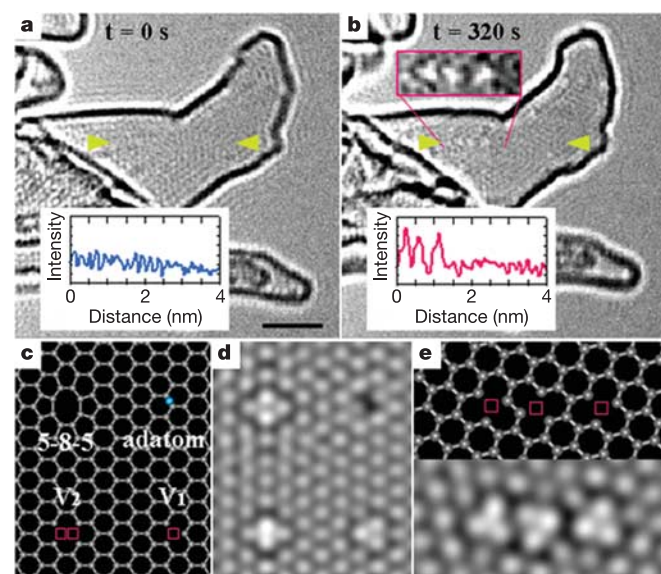 exist in carbon nanostructures for a macroscopic time under this experimental condition (at least a few seconds) even though the expected energy for vacancy formation in the graphene layer (7.0 eV in ref. 20) is rather high compared with most metals. These vacancies are immobile and do not merge together during observation. A continuous irradiation leads to a collapse of the nanotube so that the strain energy due to the vacancy formation can be relaxed.

Another important issue of the present study is to identify the carbon adatom on the graphene layer. Figure 4a shows a sequence of HR-TEM images recorded in situ on one of the SWNTs. Several dark spots and bright spots frequently appear and disappear on the SWNT during observation before it collapses (see also Supplementary Movies 2 and 3). whereas the bright spots correspond to the vacancies as described above, the dark spots should stand for carbon atoms that were knocked-on and then attached to the nanotube surface. How-ever, although these adatoms often move around and disappear during the observation, they are indeed stable for a few seconds on average during several shutter periods. Adatoms have been predicted to be mobile and to have a lower diffusion barrier (0.47 eV)[14] than that for vacancy migration (1.7 eV)[11]. Note that the adatoms appear mostly in the vicinity of the vacancies (see also Supplementary Movie 4), because this combination of vacancy and neighbouring adatom has been predicted to be metastable and long lived[4,25,26]. This is direct proof of a recombination barrier between vacancies and adatoms, which are mostly believed to remerge instantaneously when they come close to each other. In addition, more stabilized carbon adatoms on curved graphene layers are pointed out in ref. 12 and the mobility of the adatoms can be decreased in the vicinity of vacancies because of a possible off-plane relaxation, for instance.

To assign these defective structures more precisely, systematic HR-TEM image simulations have been performed for various combinations of adatom(s) and (multi-) vacancy. A best fit with one of the experimental images (Fig. 4b) extracted from Supplementary Movie 4 is shown in Fig. 4c. This structural model consists of three adatoms and one di-vacancy in a planar graphene layer. It again implies adatom mobility because the defect cannot be created locally by one (or two) knock-out events. Two contrast profiles derived from the simulated image show quantitative agreement with the experimental profiles recorded at the Scherzer defocus (Fig. 4d). Putting heavier atoms such as Fe mono-atoms
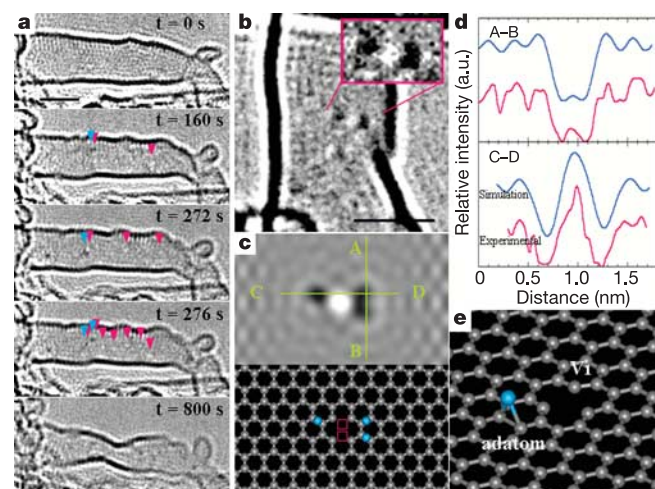

Figure 3 In situ observation of vacancy formation in a graphene layer. **a**, **b**, HR-TEM images of a single-walled carbon nanostructure recorded before electron irradiation (**a**) and after 320 s of irradiation (**b**). Intensity profiles (insets) between the two arrows illustrate the contrast measured at the carbon vacancies. **c**, **d**, Atomistic models (**c**) and simulated HR-TEM image (**d**) for a graphene layer with an adatom, unrelaxed vacancies (V_1 and V_2) and a 5–8–5 rearrangement. Squares indicate the location of the vacancy. **e**, Atomic model and simulated HR-TEM image with three mono-vacancies, giving the best match to the experimentally observed defect structures (**b**, inset). Scale bar, 2 nm.

Figure 4 In situ observation of adatom–vacancy pair formation. **a**, HR-TEM images of a SWNT during electron irradiation (the total acquisition time was ~800 s). The bright spots correspond to the vacancies (red arrows) and the dark to adatoms (blue arrows). **b**, An extracted image from Supplementary Movie 4. **c**, Simulation for three adatoms and di-vacancy model (not energetically relaxed) fits quite well with the experiment. **d**, Two contrast profiles derived from the simulation and the experimental image show quantitative agreement. **e**, The most prolific defect model with an adatom–vacancy pair (see also Supplementary Movie 2). Scale bar, 2 nm.

into the simulation (representing possible impurities from a catalyst) instead of carbon adatoms gives a considerable deviation from the experimental profiles, which supports again the notion that the defect structure involves only carbon adatoms and vacancies. The more frequent defect structure of an adatom–vacancy pair is shown schematically in Fig. 4e.

Defects in a graphene layer, such as topological defects, vacancies and adatoms, have been experimentally proved to be numerous and stable under electron irradiation. We can envisage more diversified applications in nanocarbon materials by taking advantage of these defects, which can be induced locally during electron irradiation. Combining the present experiments with the scanning probe microscopy technique and its associated electron transport measurements[27,28] is of particular interest and might allow us to obtain more comprehensive information on the physical and chemical properties of defective carbon nanostructures. □

Methods

Electron microscopy

A Schottky-type field emission gun (JEOL, JEM-2010F) was used for HR-TEM. We employed optimized parameters for imaging, well fitted to a high-efficiency charge-coupled device (CCD)-based camera (Gatan model 794) with a fibre-optic coupling to the YAG scintillators. To enhance phase contrast and decrease thermally induced drift in the specimen as much as possible, a multi-exposure procedure was employed so that we could decrease the exposure time to 1 s and sum a few images with specimen-drift corrections to limit electron irradiation damage and the consequent thermally induced structural changes, high-speed blanking was used to prevent exposure of the specimen to the electron beam during each readout by the CCD detector. A typical electron dose was ~60,000 electrons nm^{-2} for a HR-TEM image. To realize both sufficient sensitivity and sufficient resolution to visualize the single graphene layer, we used a lower accelerating voltage (120 keV) for the incident electron beam close to the displacement threshold, for the following three reasons: first, to double the scattering cross-section of carbon atoms being observed; second, so that carbon adatoms were not blasted away from the graphene layers and could therefore be observed (note that the threshold for electron irradiation on carbon materials is taken to be 80–140 keV; and last, to optimize the efficiency of the CCD detector for image acquisition. As indicated by the red graph in Supplementary Fig. S1 (bottom inset), we carefully chose the experimental conditions as a compromise with the moderate accelerating voltage of the incident electron beam so that the CTF could have a local maximum at 0.21–0.23 nm, which corresponds exactly to the repeat distance of the zig-zag chain of a graphene layer (Supplementary Fig. S1, top inset). The confidence level for the detection of a single carbon atom exceeds 80%. All the experiments shown here were performed at room temperature because raising the temperature might have led to an instantaneous relaxation of these atomic defects.

Chiral index determination

The apparent chiral angle (α) can be measured to an accuracy of ~3°; measurement of the diameter (d) in the HR-TEM image might involve about 10% error, as previously quoted in refs 15 and 29. We made a systematic study with a series of image simulations for the nanotubes of various diameters (Supplementary Fig. S3). Taking all of the microscope parameters into account, the true diameter can be therefore deduced from the apparent tube diameter to within the 3% error. The inclination of the specimen to the incident electron beam cannot be neglected in this experiment. We selected the tubes to examine which were as parallel as possible to the observed plane within a few degrees of inclination. Optical diffraction is strongly influenced by the inclination of the sample, whereas conventional electron diffraction is weakly dependent on it. The distortion and disappearance of symmetrical hexagons in optical diffraction is able to assist in the estimation of inclination angles. Our simulation tells us that the chiral angle can be measured to an accuracy of ~3° when the inclination angle is within 10°.

1. Hansson, A., Paulsson, M. & Stafström, S. Effect of bending and vacancies on the conductance of carbon nanotubes. *Phys. Rev. B* **62**, 7639–7644 (2000).
2. Ewels, C. P., Heggie, M. I. & Briddon, P. R. Adatoms and nanoengineering of carbon. *Chem. Phys. Lett.* **351**, 178–182 (2002).
3. Nordlund, K., Keinonen, J. & Mattila, T. Formation of ion irradiation induced small-scale defects on graphite surfaces. *Phys. Rev. Lett.* **77**, 699–702 (1996).
4. Krasheninnikov, A. V., Nordlund, K., Sirviö, M., Salonen, E. & Keinonen, J. Formation of ion-irradiation-induced atomic-scale defects on walls of carbon nanotubes. *Phys. Rev. B* **63**, 245405 (2001).
5. Kelly, K. F. & Halas, N. J. Determination of α and β site defects on graphite using C_{60}-adsorbed STM tips. *Surf. Sci.* **416**, L1085–L1089 (1998).
6. Ouyang, M., Huang, J.-L., Cheung, C. L. & Lieber, C. M. Atomically resolved single-walled carbon nanotube intramolecular junctions. *Science* **291**, 97–100 (2001).
7. Meyer, R. R. *et al.* A composite method for the determination of the chirality of single walled carbon nanotube. *J. Microsc.* **212**, 152–157 (2003).
8. Zuo, J. M., Vartanyants, I., Gao, M., Zhang, R. & Nagahara, L. A. Atomic resolution imaging of a carbon nanotube from diffraction intensities. *Science* **300**, 1419–1421 (2003).
9. Stone, A. J. & Wales, D. J. Theoretical studies of icosahedral C_{60} and some related species. *Chem. Phys. Lett.* **128**, 501–503 (1986).
10. Telling, R. H., Ewels, C. P., El-Barbary, A. A. & Heggie, M. I. Wigner defects bridge the graphite gap. *Nature Mater.* **2**, 333–337 (2003).
11. El-Barbary, A. A., Telling, R. H., Ewels, C. P., Heggie, M. I. & Briddon, P. R. Structure and energetics of the vacancy in graphite. *Phys. Rev. B* **68**, 144107 (2003).
12. Krasheninnikov, A. V. *et al.* Adsorption and migration of carbon adatoms on carbon nanotubes: Density-functional *ab initio* and tight-binding studies. *Phys. Rev. B* **69**, 073402 (2004).
13. Ewels, C. P., Telling, R. H., El-Barbary, A. A., Heggie, M. I. & Briddon, P. R. Metastable Frenkel pair defect in graphite: Source of Wigner energy? *Phys. Rev. Lett.* **91**, 25505 (2003).
14. Lehtinen, P. O. *et al.* Magnetic properties and diffusion of adatoms on a graphene sheet. *Phys. Rev. Lett.* **91**, 17202 (2003).
15. Kociak, M., Hirahara, K., Suenaga, K. & Iijima, S. How accurate can the determination of chiral indices of carbon nanotubes be? *Eur. Phys. J. B* **32**, 457–469 (2003).
16. Ajayan, P. M., Ravikumar, V. & Charlier, J.-C. Surface reconstructions and dimensional changes in single-walled carbon nanotubes. *Phys. Rev. Lett.* **81**, 1437–1440 (1998).
17. Smith, B. W. & Luzzi, D. E. Electron irradiation effects in single wall carbon nanotubes. *J. Appl. Phys.* **90**, 3509–3515 (2001).
18. Iijima, S. *et al.* Nano-aggregates of single-walled graphitic carbon nano-horns. *Chem. Phys. Lett.* **309**, 165–170 (1999).
19. Yakobson, B. I., Samsonidze, G. & Samsonidze, G. G. Atomistic theory of mechanical relaxation in fullerene nanotubes. *Carbon* **38**, 1675–1680 (2000).
20. Banhart, F. Irradiation effects in carbon nanostructures. *Rep. Prog. Phys.* **62**, 1181–1221 (1999).
21. Hahn, J. R., Kang, H., Song, S. & Jeon, I. C. Observation of charge enhancement induced by graphite atomic vacancy: A comparative STM and AFM study. *Phys. Rev. B* **53**, R1725–R1728 (1996).
22. Orlikowski, D., Buongiorno Nardelli, M., Bernholc, J. & Roland, C. Theoretical STM signatures and transport properties of native defects in carbon nanotubes. *Phys. Rev. B* **61**, 14194–14203 (2000).
23. Asari, E., Kitajima, M., Nakamura, K. G. & Kawabe, T. Thermal relaxation of ion-irradiation damage in graphite. *Phys. Rev. B* **47**, 11143–11148 (1993).
24. Hjort, M. & Stafström, S. Modeling vacancies in graphite via the Hückel method. *Phys. Rev. B* **61**, 14089–14094 (2000).
25. Krasheninnikov, A. V., Nordlund, K. & Keinonen, J. Production of defects in supported carbon nanotubes under ion irradiation. *Phys. Rev. B* **65**, 165423 (2002).
26. Lu, A. J. & Pan, B. C. Nature of single vacancy in achiral carbon nanotubes. *Phys. Rev. Lett.* **92**, 105504 (2004).
27. Wildöer, J. W. G., Venema, L. C., Rinzler, A. G., Smalley, R. E. & Dekker, C. Electronic structure of atomically resolved carbon nanotubes. *Nature* **391**, 59–62 (1998).
28. Odom, T. W., Huang, J.-L., Kim, P. & Lieber, C. M. Atomic structure and electronic properties of single-walled carbon nanotubes. *Nature* **391**, 62–64 (1998).
29. Kociak, M. *et al.* Linking chiral indices and transport properties of double-walled carbon nanotubes. *Phys. Rev. Lett.* **81**, 155501 (2002).

....

Chemical remodelling of cell surfaces in living animals

Jennifer A. Prescher[1]*, Danielle H. Dube[1]* & Carolyn R. Bertozzi[1,2]

[1]*Department of Chemistry, University of California, Berkeley, California 94720, USA*
[2]*Department of Molecular and Cell Biology and Howard Hughes Medical Institute, University of California, Materials Sciences Division, Lawrence Berkeley National Laboratory, Berkeley, California 94720, USA*

* These authors contributed equally to this work

....

Cell surfaces are endowed with biological functionality designed to mediate extracellular communication. The cell-surface repertoire can be expanded to include abiotic functionality through the biosynthetic introduction of unnatural sugars into cellular glycans, a process termed metabolic oligosaccharide engineering[1,2]. This technique has been exploited in fundamental studies of glycan-dependent cell–cell and virus–cell interactions[3–5] and